Journal of Zhejiang University-SCIENCE A
www.jzus.zju.edu.cn; www.springer.com/journal/11582
E-mail: jzus_a@zju.edu.cn

Research Article
https://doi.org/10.1631/jzus.A2500625

Rapid, material-aware inverse design of one-dimensional photonic crystals using a mixture-of-physics-expert framework

Haoming LI*, Zhiyuan ZHOU*, Xinzi LIN, Wuyong QU, Dongxu JI✉

School of Science and Engineering, The Chinese University of Hong Kong, Shenzhen, Shenzhen 518172, China

Abstract: In this work, we present an unsupervised physics-informed neural network (PINN) framework for the inverse design of 1D photonic crystals, addressing the limitations of conventional methods, such as high computational cost and inability to optimize materials. A "mixture-of-physics-expert" method for nanophotonic design is proposed, which pretrains a library of PINN models for various material combinations. This allows for not only rapid structure optimization directly from target spectra, even hand-drawn ones, but also efficient selection of the optimal material system for a given task, which is a capability traditional algorithms lack. By embedding physical governing equations as a loss constraint, our framework eliminates the need for large labeled data and enhances physical explainability. As a practical demonstration, we apply this framework to design a spectral-splitting optical filter for a high-bandgap/low-bandgap hybrid photovoltaic system. We compare designs from five pretrained material-specific PINN models and identify the optimal material configuration that enhances the overall photovoltaic system efficiency by 22.4% compared with a standalone GaAs solar cell and 41.9% compared with a GaInP cell. Notably, the designed filters exhibit excellent angular robustness with only 3.5% relative efficiency degradation at 45° oblique incidence and significantly reduce the operating temperature of low-bandgap cells by 12.8–14.6 °C. This physics-guided and material-aware framework establishes a new paradigm for photonic device design, balancing computational efficiency, design flexibility, and practical applicability.

Key words: Photonic crystals; Physics-informed neural network (PINN); Mixture-of-physics-expert model; Thin film

1 Introduction

Multilayer one dimensional photonic crystals (1D-PhCs) are vital in optics and energy engineering (Li JL et al., 2024; Li HM et al., 2025; Yu et al., 2025). One dimensional PhCs operate by introducing a structure with periodic variation in the refractive index along a single spatial dimension, therefore enabling precise control over the light flow (Wan et al., 2021). This capability has made 1D-PhCs indispensable in a variety of applications, including optical filters for thermophotovoltaics (Ma et al., 2025), spectral splitting for photovoltaic systems (Qu et al., 2025), and biosensing (Pavlichenko et al., 2015). Effective design of a 1D-PhC that features a required behavior involves exploring a vast parameter space, including material choices, layer thicknesses, and refractive index contrasts. The high level of flexibility poses a significant challenge for the inverse design methodology of 1D-PhCs (Luce et al., 2023).

Traditional inverse design for nano-photonics relies heavily on gradient-based approaches or evolutionary optimization (Molesky et al., 2018). The core principle of these traditional methods is defining and using a physics-based forward model to guide the optimization. For instance, the transfer matrix method (TMM) is a typical physics-based forward model (Hecht, 2021; Luce et al., 2022). This model takes the PhC parameters as inputs, such as refractive indices and thicknesses of layers, outputs the response spectrum of the current PhC structure. The iterative gradient descent method (Anzengruber et al., 2012) calculates the gradient of the PhC response spectrum with respect to the refractive index distribution and uses the gradient to minimize the difference between the PhC design response spectrum and the target spectrum.

✉ Dongxu JI, jidongxu@cuhk.edu.cn
* The two authors contributed equally to this work
Dongxu JI, https://orcid.org/0000-0003-3743-0939

Received Nov. 29, 2025; Revision accepted Mar. 16, 2026;
Crosschecked Aug. 22, 2026

© Zhejiang University Press 2026

The main drawbacks of the iterative gradient descent method are local optima and high computational cost. In contrast, heuristic optimization algorithms, such as the genetic algorithm (GA) (Schubert et al., 2008; Liu et al., 2024), particle swarm optimization (PSO) (Ruan et al., 2016; Lee et al., 2023), and the needle method (Tikhonravov et al., 1996, 2007), have better global optimization capabilities, effectively overcoming local optima entrapment while exploring the design space. Apart from merely optimizing the PhC structure, the GA can also inversely design the material and total layer number (Kim et al., 2021). Nevertheless, the traditional methods are more suitable for the "one-task-one-calculation" scenario. They require starting from scratch for each task, and the computational cost of heuristic optimization algorithms remains prohibitively high, especially for inverse design tasks involving 1D-PhCs with numerous layers. Predicting structures that generate a spectrum sufficiently matching the target spectrum within a reasonable time becomes difficult or even practically infeasible (Lininger et al., 2021; Zhan et al., 2022). Hence, a fast and adaptable inverse design method is needed for more complicated 1D-PhC design tasks.

Compared with traditional inverse design methods, the artificial intelligence (AI) method enables higher computational efficiency (Wang et al., 2024). A variety of deep learning methods have been applied to efficiently solve the inverse design problem of 1D-PhCs, such as fully connected networks (FCNs) (Liu et al., 2018), convolutional neural networks (CNNs) (Lininger et al., 2021), conditional invertible neural networks (CINNs) (Luce et al., 2023), variational autoencoders (VAEs) (Hong and Nicholls, 2022), and Transformers (Ma et al., 2024). Nevertheless, the deep learning methods mentioned above are based on purely data-driven supervised learning, which suffers from two major limitations: (a) reliance on extensive labeled data comprising real-world spectral data and photon crystal structures; (b) the absence of physical explainability. To obtain an efficient deep learning model, the researcher must generate numerous 1D-PhC structures as the training labels (ground truths) alongside their corresponding optical response spectra as the training data. Thousands to tens of millions of real-world structures and spectra are typically used to train the models in previous relevant studies, which leads to a significantly large computational cost (Lininger et al., 2021; Hong and Nicholls, 2022; Luce et al., 2023; Ma et al., 2024). Moreover, it has been widely reported that models trained on real-world data struggle with tasks beyond their training domain, particularly in tasks of inverse PhC design, where target spectra are often idealized step-like profiles that do not exist in either practical scenarios or real-world training data (Wang HZ et al., 2021; Luce et al., 2023; Wang QZ et al., 2024). This mismatch between the training data and tasks significantly limits the performance and generalization ability of the data-driven model. Another critical issue of traditional data-driven deep learning models is the black box problem (Pedreschi et al., 2019), which suggests that the current data-driven deep learning models lack physical explainability.

To address the above problem of traditional data-driven AI models, many studies have advocated for the adoption of more explainable AI models (Jiménez-Luna et al., 2020; Ahmed et al., 2022; Wang et al., 2022). As a type of explainable AI model, the physics-informed neural network (PINN) has been introduced in various recent studies (Chen et al., 2020; Chen and Dal Negro, 2022; Khatib et al., 2022; Zhelyeznyakov et al., 2023; Medvedev et al., 2025; Riganti et al., 2025; Zhu et al., 2025) to solve optical inverse problems. Unlike pure data-driven models that depend on labels, PINN integrates physical governing equations as regularization constraints during training, effectively embedding prior physics knowledge into the optimization process through residual loss functions (Medvedev et al., 2025). This strategy significantly enhances the prediction accuracy and accelerates network convergence in intelligent metasurfaces (You et al., 2024). The adoption of physical constraints reduces the parameter search space and guides gradient backpropagation in network training, allowing neural networks to learn complex mappings with less reliance on large amounts of data. Furthermore, the PINN (Khatib et al., 2022) achieves a significantly lower error compared to the traditional data-driven network in electromagnetic response prediction tasks that fall outside the training data distribution space, with a reduction of 36% in parameter scale compared to a traditional data-driven network.

To demonstrate the practical utility of our framework, we apply it to design spectral-splitting filters for hybrid photovoltaic systems. While single-junction cells face fundamental Shockley–Queisser efficiency limits (Rühle, 2016), multijunction architectures suffer from

current-matching constraints and fabrication complexity that compromise reliability (Rahman et al., 2025). Spectral-splitting photovoltaic (SSPV) systems circumvent these issues by spatially separating subcells to absorb specific spectral bands without electrical interconnection (Dorodnyy et al., 2015; Yu et al., 2015; Jiang et al., 2019; Ahmadi et al., 2025; Zhu et al., 2025). However, existing SSPV filter designs rely on computationally expensive iterative optimizations. We address this bottleneck by developing a differentiable TMM that embeds physical laws directly into PINN training without requiring labeled data. Our key innovation is a "mixture-of-physics-expert" (MOPE) strategy, which is analogous to a "mixture-of-expert" (MOE) model in the large language model field. We pretrain specialized PINN models for distinct material combinations, conduct parallel inference of the PINN model, and choose the best material combination and PhC structure, enabling rapid material-system selection and structure optimization that traditional algorithms cannot achieve.

2 Methodology

The inverse design problem can be formulated as an input–output mapping. As shown in Figs. 1a and 2, the model takes the target reflectance spectrum as the input and predicts the corresponding 1D-PhC structure as the output. The structure is represented as an l-dimensional vector $\boldsymbol{d}=[d_1, d_2, \cdots, d_l]$, where d_i (i=1, 2, ⋯, l) is the thickness of the ith layer, and l is the number of layers. The target spectrum is a vector $\boldsymbol{r}=[r_1, r_2, \cdots, r_k]$, where r_j (j=1, 2, ⋯, k) is the reflectance of the jth wavelength sampling point, and k is the number of sample points, as shown in Fig. 1a. Three cases were conducted in this study to comprehensively evaluate the performance of the proposed PINN framework: Case 1 compares PINN and data-driven CNN, training with a real-world data of TiO_2–SiO_2 structures; Case 2 evaluates eight PINN models with different material combinations on various optical filter design tasks; Case 3 applies the MOPE framework to design spectral-splitting filters for hybrid photovoltaic systems. The detailed experimental setup for each case is described in Section 3. Fig. 1b illustrates the concept of the SSPV system. Incident sunlight first encounters the 1D-PhC dichroic filter, which functions as a spectral

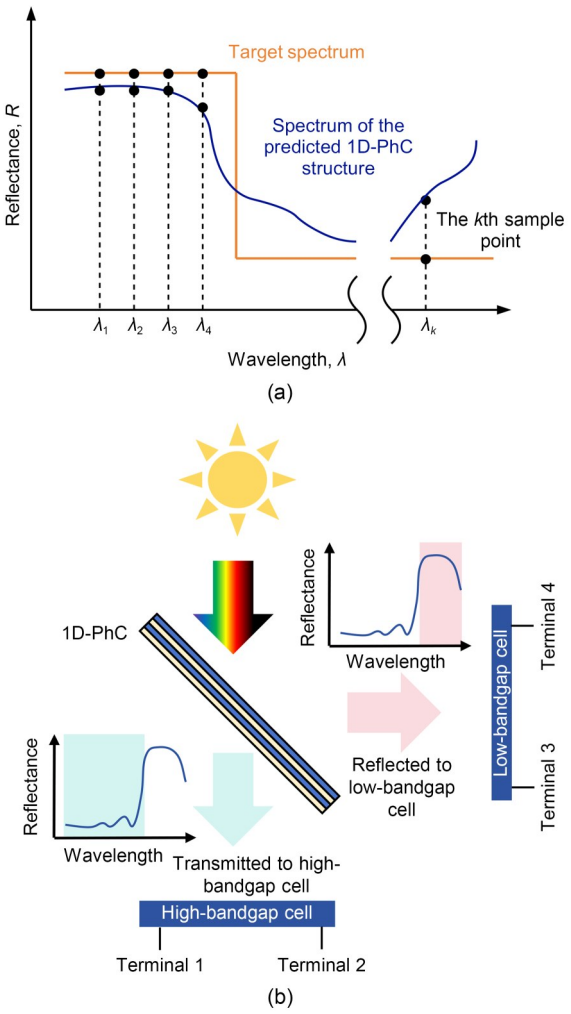


Fig. 1 (a) Example of the sampling of the ideal target spectrum and spectrum of the predicted 1D-PhC structure; (b) illustration of the concept of an SSPV system. λ_j (j=1, 2, ⋯, k) is the wavelength of the jth sample point

beam splitter. The filter is designed to transmit photons with wavelengths shorter than the cut-off wavelength to the high-bandgap cell (GaAs or GaInP) while reflecting photons with wavelengths longer than the cut-off wavelength to the low-bandgap cell (Si). The high- and low-bandgap cells are spatially separated from each other, and they are electrically isolated, with no series or parallel connections between their respective electrode terminals. This spectral separation strategy enables each photovoltaic cell to operate within its optimal spectral range, minimizing thermalization losses in the high-bandgap cell and sub-bandgap transmission losses in the low-bandgap cell. The combined system thus achieves higher overall efficiency than either standalone cell alone.

2.1 Structure of the physics-informed neural network

The structure of the PINN model in this study is based on a typical convolutional architecture shown in Fig. 2. The network consists of two parts: the feature learning part and the numerical regression part. The feature learning part accepts the input target spectrum ***r***, with convolutional layers and maxpooling layers alternating in a sequential manner to extract a series

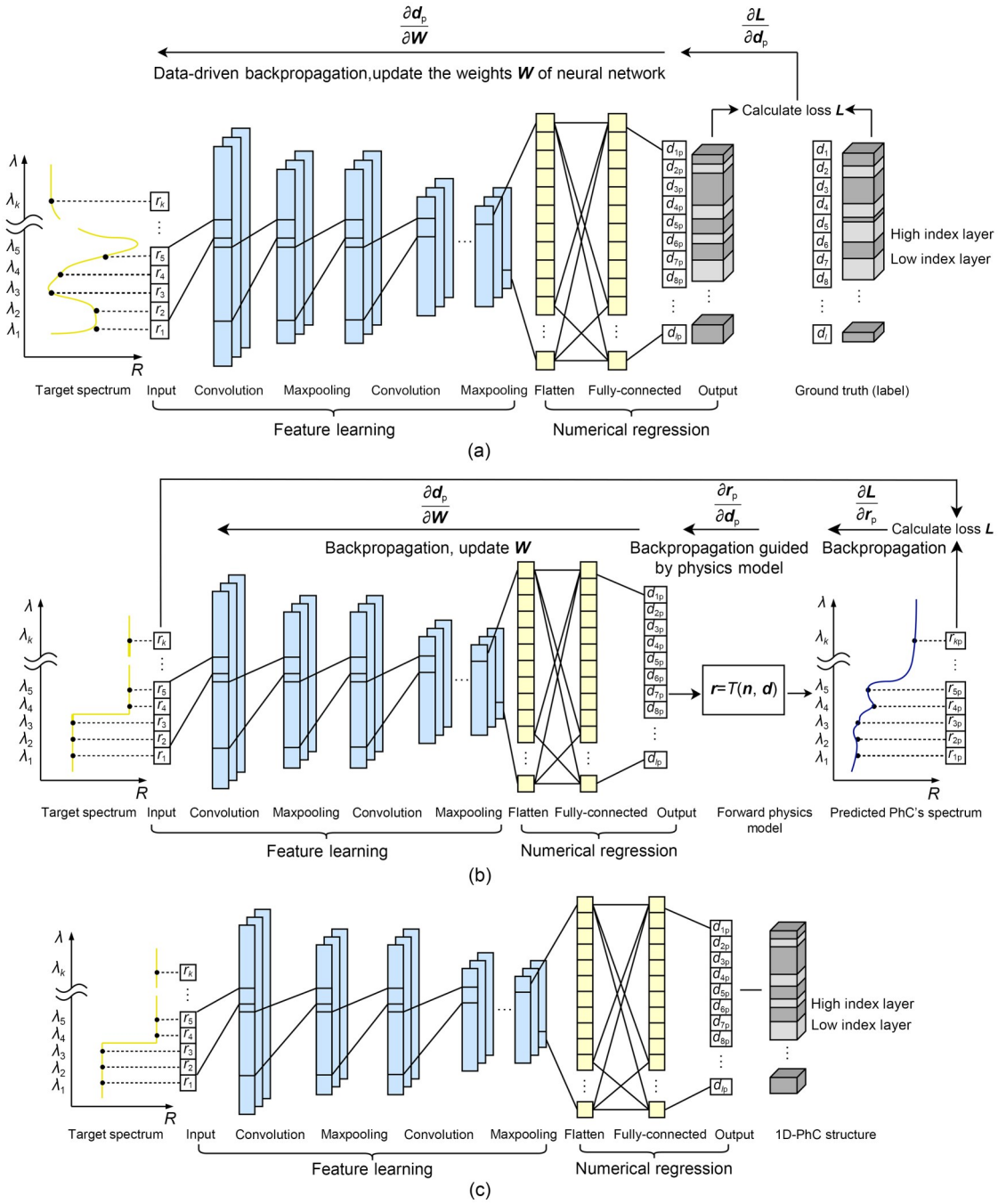


Fig. 2 (a) Supervised data-driven training of CNN; (b) unsupervised training of the PINN; (c) inference of the PINN or CNN. $r_p=[r_{1p}, r_{2p}, \cdots, r_{kp}]$ is the spectrum vector of the predicted 1D-PhC structure, where r_{jp} (j=1, 2, ⋯, k) is the reflectance at the sample point j; $d_p=[d_{1p}, d_{2p}, \cdots, d_{lp}]$ is the structure vector of the predicted 1D-PhC, where d_{ip} (i=1, 2, ⋯, l) is the thickness of the ith layer in the 1D-PhC. T is the differentiable forward physics model; n is the vector of preset refractive indices of the PhC layers, which correspond to the preset film material configuration

of features from the target spectrum while reducing spatial dimensions. The numerical regression part predicts the thickness of each layer in the 1D-PhC. Specifically, after flattening the feature maps from the last layer of the feature learning component into a 1D vector, a series of fully connected layers maps these features to the desired output dimensions. The final layer outputs a 1D vector $\boldsymbol{d}_{\mathrm{p}}$, representing the thicknesses of individual layers in the 1D-PhC.

2.2 PINN training

In the training process, as shown in Fig. 2b, we use the ideal spectra as the training data, and the model predicts the structures of the 1D-PhCs corresponding to these spectra. Then, a differentiable forward physics model mentioned above takes the predicted structures $\boldsymbol{d}_{\mathrm{p}}$ and calculates their response spectra $\boldsymbol{r}_{\mathrm{p}}$:

$$\boldsymbol{r}_{\mathrm{p}}=T(\boldsymbol{n},\ \boldsymbol{d}_{\mathrm{p}}). \tag{1}$$

The loss function $\boldsymbol{L}_{\mathrm{PINN}}$ of PINN training can be described as:

$$\boldsymbol{L}_{\mathrm{PINN}}=\alpha\cdot\boldsymbol{L}_{\mathrm{MSE}}+\beta\cdot\sum_{i=1}^{11}\boldsymbol{L}_{\mathrm{reg},i}, \tag{2}$$

where $\boldsymbol{L}_{\mathrm{MSE}}$ is the mean square error (MSE) between the input ideal spectra $\boldsymbol{r}$ and the spectra of the predicted 1D-PhC structure $\boldsymbol{r}_{\mathrm{p}}$; $\boldsymbol{L}_{\mathrm{reg},i}$ is the regulation loss function for restraining the thickness of each layer within the range of 0.02–0.30 μm; α and β are the weight coefficients. The regulation loss function can be found in Section S2 of the electronic supplementary materials (ESM). $\boldsymbol{L}_{\mathrm{MSE}}$ is calculated by Eq. (3):

$$\boldsymbol{L}_{\mathrm{MSE}}=\frac{1}{B}\sum_{b=1}^{B}\frac{1}{k}\sum_{j=1}^{k}\left(r_{j\mathrm{p}}^{b}-r_{j}^{b}\right)^{2}, \tag{3}$$

where B and b are the batch size and the ordinal number of data in the mini batch, respectively; k is the number of wavelength sample points on the spectra and is fixed to 161 in this work; $r_{j\mathrm{p}}^{b}$ is the reflectance of the jth sample point of the predicted 1D-PhC spectrum in the bth mini batch; r_{j}^{b} is the reflectance of the jth sample point of the input spectrum in the bth mini batch.

Unlike conventional data-driven approaches requiring explicit ground-truth structures as labels and corresponding spectra as training data, the PINN method utilizes input spectra dually as both training data and labels. Crucially, these training spectra accommodate both experimentally measured data (with known physical structures) and idealized forms, including analytically defined curves. This dual functionality offers flexibility in training data acquisition and better generalization ability. The backpropagation and PINN weight update follow Eq. (4):

$$\frac{\partial\boldsymbol{L}}{\partial\boldsymbol{W}}=\frac{\partial\boldsymbol{L}}{\partial\boldsymbol{r}_{\mathrm{p}}}\cdot\frac{\partial\boldsymbol{r}_{\mathrm{p}}}{\partial\boldsymbol{d}_{\mathrm{p}}}\cdot\frac{\partial\boldsymbol{d}_{\mathrm{p}}}{\partial\boldsymbol{W}}. \tag{4}$$

The physics model guides the gradient backpropagation (Fig. 2b), and details about the differentiable forward physics model can be found in Section S1 of the ESM.

2.3 Data-driven CNN training

A CNN model is trained in parallel using the data-driven training method to compare with the PINN model. The neural network structure of the CNN is the same as that of the PINN, and the training method is illustrated in Fig. 2a. A large number of 1D-PhC structures $\boldsymbol{d}$ are generated as the training labels, and their corresponding reflectance spectra $\boldsymbol{r}$ are obtained as the input training data.

The loss function $\boldsymbol{L}_{\mathrm{CNN}}$ of CNN training is defined as:

$$\boldsymbol{L}_{\mathrm{CNN}}=\gamma\cdot\frac{1}{B}\sum_{b=1}^{B}\frac{1}{l}\sum_{i=1}^{l}\left(d_{i\mathrm{p}}^{b}-d_{i}^{b}\right)^{2}+\delta\cdot\sum_{i=1}^{l}\boldsymbol{L}_{\mathrm{reg},i}, \tag{5}$$

where $d_{i\mathrm{p}}^{b}$ is the predicted thickness of the ith layer in the bth mini batch; d_{i}^{b} is the true thickness of the ith layer in the label in the bth mini batch; l is the total number of layers in the 1D-PhC, which is set to 11 or 9 in this study; γ and δ are the weight coefficients. The regulation function for CNN training is the same as that for PINN training, which is described in Section S2 of the ESM. The training hyperparameters are set to be consistent for both the PINN and CNN to ensure the fairness of the comparison. The detailed training settings are listed in Section S3 of the ESM.

3 Experimental design and data preparation

Three cases were conducted in the experiment to analyze the performance of the CNN and PINN methods.

Case 1: the data-driven CNN and PINN were trained, validated, and compared based on the same real-world data to analyze the impact of physics information on the training process. Real-world data was constructed, including 12800 randomly generated 11-layer TiO_2–SiO_2 periodic 1D-PhC structures and their corresponding reflectance spectra calculated by TMM. The thickness of each layer in the randomly generated structures was set to range from 0.02 to 0.30 μm. The data were split into training data (80%, 10240 pairs of 1D-PhC structures and spectra), validation data (12%, 1536 pairs of 1D-PhC structures and spectra), and test data. The performance of both models was evaluated in each training epoch by predicting the 1D-PhC structures corresponding to the validation spectra, feeding the predicted structures into TMM to compute the reflectance spectra, and recording the mean absolute error (MAE) between the predicted and ground-truth spectra. The convergence behavior of each method during training was monitored based on the calculated MAE.

Case 2: eight PINN models with eight distinct material combinations were trained to investigate the material-dependent predictive capabilities of the proposed model. 1D-PhCs typically feature periodic structures composed of materials with varying refractive indices. While some studies use only two materials (e.g., high–low refractive index pairs), others employ multiple material configurations. In this experiment, eight commonly used material configurations were selected: TiO_2–Al_2O_3, TiO_2–SiO_2, Ta_2O_5–SiO_2, Ta_2O_5–Al_2O_3, TiO_2–Ta_2O_5, Al_2O_3–SiO_2, TiO_2–Ta_2O_5–Al_2O_3–SiO_2, and TiO_2–SiO_2–Ta_2O_5–Al_2O_3. Specific material sequences can be found in Section S4 of the ESM. The refractive indices of materials are also given in Section S6 of the ESM.

The training data in Case 2 were a group of ideal spectra, such as the yellow spectrum in Fig. 1. The total number of ideal spectra for training was 2250. All eight models were trained based on the same group of ideal spectra. Post-training evaluations were conducted by employing these models for eight distinct inverse design tasks, such as optical longpass filters, band notch filters, bandpass filters, and shortpass filters. The target spectra of the tasks were independent of the training data.

Case 3: application in SSPV system design. To demonstrate the practical utility of the MOPE framework, we tasked our pretrained models with a real-world challenge: designing a nine-layer spectral-splitting filter for an SSPV system. We selected five promising material combinations from the library: TiO_2–Al_2O_3–MgF_2, TiO_2–Al_2O_3, TiO_2–MgF_2, TiO_2–SiO_2–MgF_2, and TiO_2–SiO_2. The detailed material configurations are listed in Section S5 of the ESM. Each corresponding PINN model was used to inversely design a filter structure based on ideal spectral-splitting target spectra. The performance of these uniquely designed filters was then evaluated by simulating their impact on the total power output of two different tandem photovoltaic systems: a GaAs/Si system and a GaInP/Si system. This case is designed to showcase our method's ability to not only generate device structures rapidly but also to facilitate the selection of the best material system for a specific application by comparing end-to-end system performance. The performances of GaAs and Si cells are calculated by the single-diode model, while GaInP is simulated by the double-diode model since the single-diode parameters of GaInP cells are rarely reported in the literature, and the single- or double-diode parameters of Si, GaAs, and GaInP cells utilized in this work are listed in Section S11 of the ESM. The current–voltage (J–V) curves can be calculated by the diode models, and the maximum power point can be found on the J–V curves. Then, the output power from each cell can be calculated. The detailed calculation process of the single- and double-diode models can be found in Sections S9 and S10 of the ESM as well.

4 Results and discussion

4.1 Case 1: impact of physics information in model training

As discussed in Section 2, the differentiable TMM is used as a part of the loss function to train the PINN model. In contrast, the loss function of the data-driven models only consists of the regulation of layer thicknesses and the MSE between the predicted PhC layer thicknesses and the target thicknesses. The MAE between the predicted 1D-PhC structure spectra and the target spectra every 50 epochs is shown in Fig. 3. This indicates that the validation loss of the PINN decreases rapidly from approximately 0.312 to 0.130 during the 0–100 epochs, and then converges at approximately 0.121 after 650 epochs, whereas the validation loss of the data-driven CNN decreases more slowly, converging

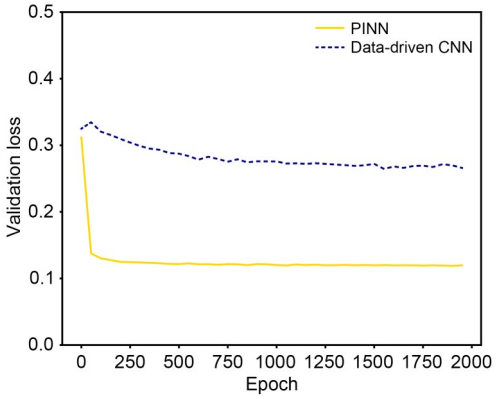


Fig. 3 Comparison of the validation losses of the PINN and data-driven CNN during the training process

at approximately 0.269 after 950 epochs. At the end of the training, the validation loss of the PINN is 0.121, which is 54.5% lower than that of the data-driven CNN, with a validation loss of 0.266.

The better convergence behavior and prediction accuracy of the PINN model can be attributed to two key mechanisms that fundamentally differentiate it from the data-driven CNN. First, integrating the differentiable TMM as a physics-informed constraint during back-propagation introduces a directional guidance mechanism for gradient updates. This physical model acts as a prior knowledge layer, effectively narrowing the weight search space by aligning the optimization trajectory with the intrinsic electromagnetic response characteristics of 1D-PhC structures. In contrast, the weights of the CNN are updated based on a purely data-driven "trial-and-error" mechanism. Second, the PINN directly uses the response spectrum in the training data as the training target, bypassing the need for intermediate structural labels. The end-to-end and target-oriented approach of PINN ensures that the predicted 1D-PhC structures prioritize matching the desired optical response over pursuing structural features, leading to higher accuracy. These advantages collectively explain why the PINN achieves a 54.5% lower validation loss than the data-driven model. In contrast, the CNNs' reliance on layer thickness regulation as an indirect surrogate for spectral control may compromise precision.

4.2 Case 2: material-dependent predictive capabilities

As shown in Fig. 4, eight models with different groups of materials were used to predict the 1D-PhC structures from eight ideal target reflectance spectra: Task 1/2: bandpass (short/long cut-off wavelength); Task 3/4: longpass (short/long cut-off wavelength); Task 5/6: band notch (short/long cut-off wavelength); Task 7/8: shortpass (short/long cut-off wavelength). The predicted 1D-PhC structures can be found in Section S7 of the ESM.

The eight target spectra were carefully chosen to cover the majority of representative optical filters. The similarity between the predicted 1D-PhC structure's reflectance spectrum and the target spectrum reveals the model's performance on the particular task. For instance, it can be easily inferred from Figs. 4f1–4f8 that the Al_2O_3–SiO_2 model is unsuitable for all eight tasks since the peak intensities of the response spectra are below 0.5, whereas the reflectance of the target spectra at the same wavelength is 1.0, and the spectral bandwidths of the peaks are also narrower than those of the target spectra. This finding is consistent with expectations. According to dielectric film theory (Hecht, 2021), the achievable reflectance and peak spectral bandwidth are fundamentally constrained by the difference between material refractive indices; therefore, the limited refractive index difference between the high-index material (Al_2O_3, n_H: approximately 1.62) and low-index material (SiO_2, n_L: approximately 1.46) results in an intrinsic performance limitation. In contrast, it is observed that the TiO_2–SiO_2 model, as shown in Figs. 4b1–4b8, has a satisfying response spectrum on the tasks among all material combinations because the refractive index difference between TiO_2 (n_H: approximately 2.38) and SiO_2 (n_L: approximately 1.46) is the highest among all eight preset material models. Nevertheless, some models have generated similar response spectra on the same task, such as Figs. 4b3 and 4c3, and the model performance cannot be evaluated solely by overlooking the spectra.

To further distinguish the predictive capabilities of eight preset material models, the model performance is further quantified by calculating the MAEs between the predicted and target spectra, and the results are presented in Fig. 5. The TiO_2–SiO_2 model achieves the lowest MAEs among all preset material models on nearly all inverse design tasks, apart from Task 3. The average MAEs of the TiO_2–SiO_2 and Al_2O_3–SiO_2 models are 0.12 and 0.39, respectively, representing the best and worst predictive performances among all preset material models. Notably, neither the TiO_2–Ta_2O_5–Al_2O_3–SiO_2 model nor the TiO_2–SiO_2–Ta_2O_5–Al_2O_3 model

exhibits better overall performance than the TiO_2–SiO_2 model, and their MAEs are 0.31 and 0.17, respectively, despite having more varied material collocations. These findings reveal that the diversification of material combinations in some inverse design problems may not necessarily lead to improved performance. Therefore, the combination of TiO_2 and SiO_2 alone may suffice for achieving comparable performance in inverse design problems within the visible light spectrum.

Additionally, an interesting pattern is noted in Fig. 5a that several inverse design tasks, such as long-pass (short cut-off wavelength) and band notches, are

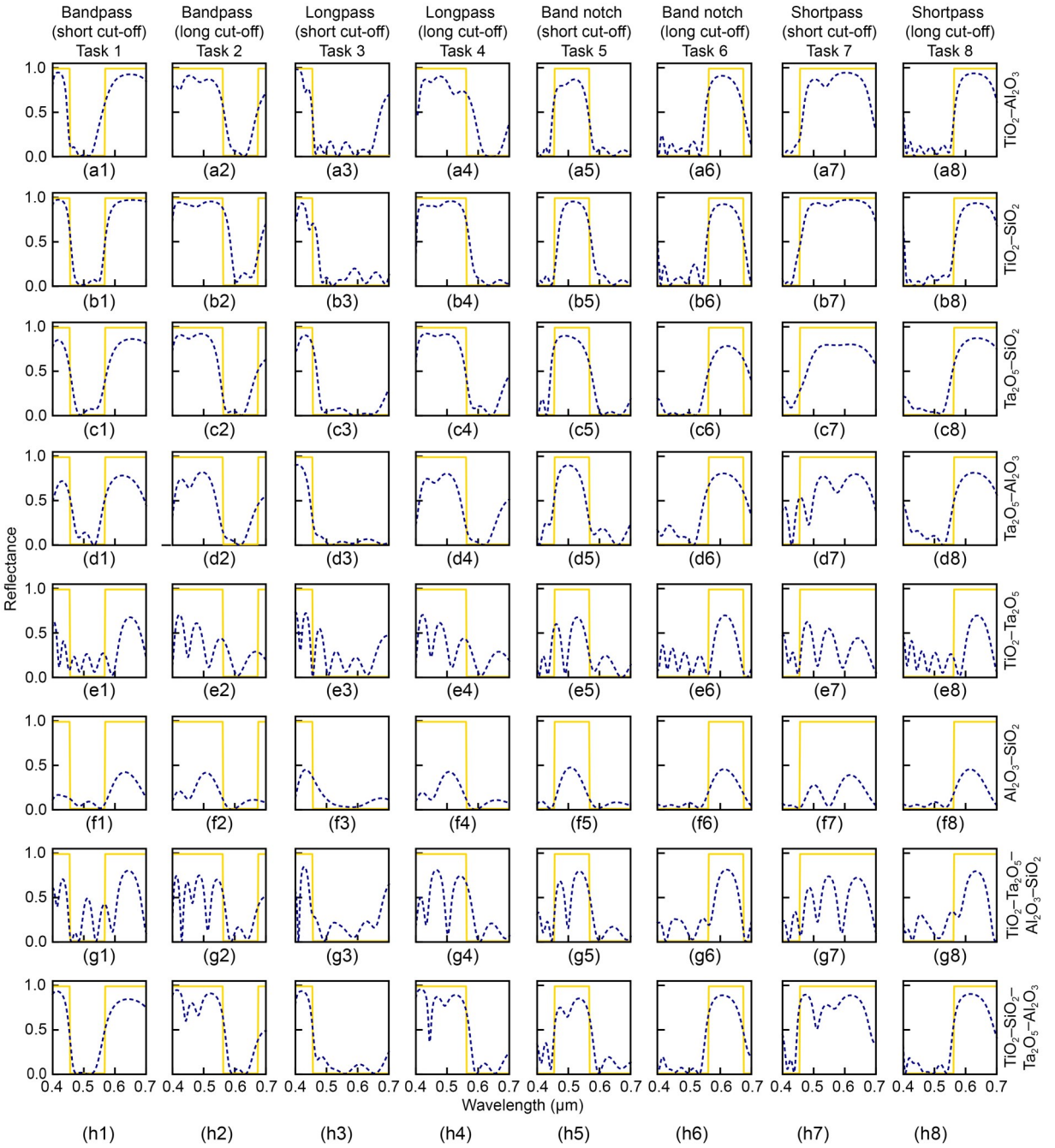


Fig. 4 Performance comparison of eight models trained with distinct material configurations: (a1–a8) TiO_2–Al_2O_3; (b1–b8) TiO_2–SiO_2; (c1–c8) Ta_2O_5–SiO_2; (d1–d8) Ta_2O_5–Al_2O_3; (e1–e8) TiO_2–Ta_2O_5; (f1–f8) Al_2O_3–SiO_2; (g1–g8) TiO_2–Ta_2O_5–Al_2O_3–SiO_2; (h1–h8) TiO_2–SiO_2–Ta_2O_5–Al_2O_3. Blue curves are the model-predicted structure spectra, and yellow lines are the target spectra

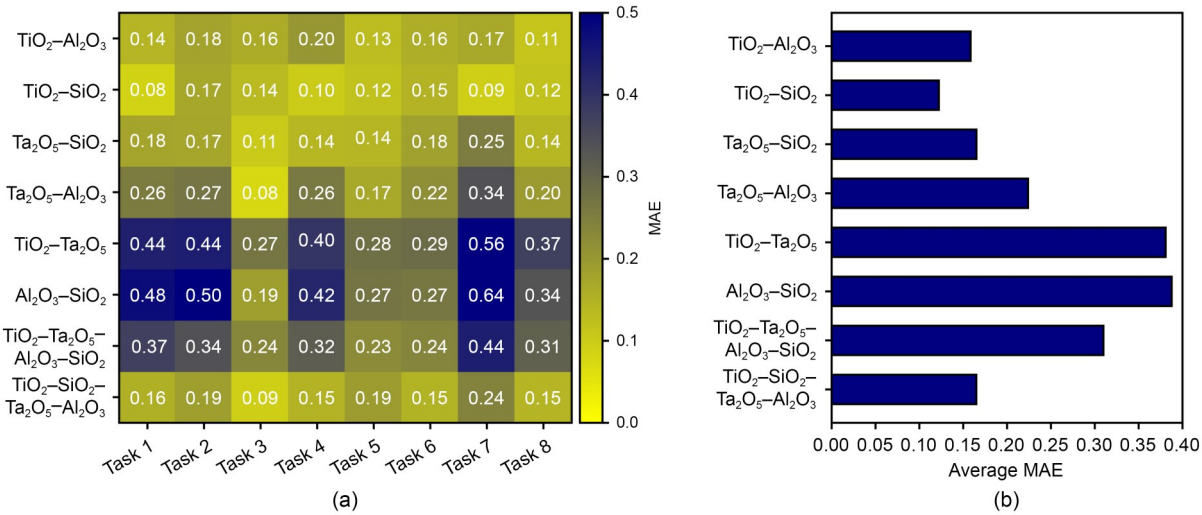


Fig. 5 (a) Heatmap of MAEs between the predicted and target spectra for 1D-PhCs across eight preset material models and eight spectral-design tasks; (b) average MAEs between the predicted and target spectra for 1D-PhCs, calculated across all eight spectral-design tasks

relatively easy for nearly all preset material models. The average MAEs across all models for these three tasks are 0.16, 0.19, and 0.21, respectively. A possible explanation is that the target spectra of these tasks feature a significantly higher proportion of regions where the reflection coefficient is 0, which reduces the difficulty for the models in predicting appropriate 1D-PhC structures. Another observation, contrarily supports our previous explanation. The shortpass (short cut-off wavelength) task, which exhibits the largest proportion of reflectance of 1 spectral region among all tasks, is proven to be the most challenging for all preset material models, leading to one of the highest average MAEs of 0.34. Nevertheless, the preset TiO_2–SiO_2 model reaches a considerably low MAE of 0.09 for this inverse design task. This finding further validates our earlier conclusion that the combination of TiO_2 and SiO_2 may be adequate for most tasks within the 400–700 nm spectral band.

4.3 Case 3: design of a dichroic filter for an SSPV system

After validating the efficiency of the PINN approach and demonstrating its capability in handling various material systems, we now apply our framework to a practical engineering problem: designing a dichroic filter for an SSPV system. In this case, five different sets of material configurations are selected to design an optic filter for combined photovoltaic cells. The cut-off wavelength is adjustable to match different combined cells. The first system utilized a GaAs/Si system, requiring the filter's cut-off wavelength to be set near 0.86 μm. The second system, leveraging the wider bandgap of GaInP, employed a GaInP/Si structure, for which the filter's cut-off wavelength was 0.72 μm. To fairly evaluate the system performance under practical operating conditions, simulations are conducted at both normal incidence (0°) and oblique incidence (45°), with the latter representing the actual operating angle for the dichroic splitter in the spectral-splitting configuration shown in Fig. 1b. The predicted 1D-PhC structures can be found in Section S8 of the ESM.

4.3.1 GaAs/Si system performance

Analysis of the predicted reflectance spectra for the GaAs/Si system at 0° incidence (Fig. 6) reveals distinct performance characteristics among the five material combinations. Notably, the filters designed using TiO_2–Al_2O_3 and TiO_2–SiO_2 exhibit exceptionally sharp transitions at the cut-off wavelength, which is critical for efficient spectral separation. A critical observation is the behavior of the reflectance in the long-wavelength regime. Unlike the other four sets, which maintain a high reflectance close to the ideal value, set TiO_2–Al_2O_3 exhibits a distinct roll-off in reflectance, as shown in Fig. 6b. One possible reason for this phenomenon is that the refractive index difference between TiO_2 and Al_2O_3 is the smallest among these combinations of materials. This performance degradation is attributed to the lower refractive index contrast between TiO_2

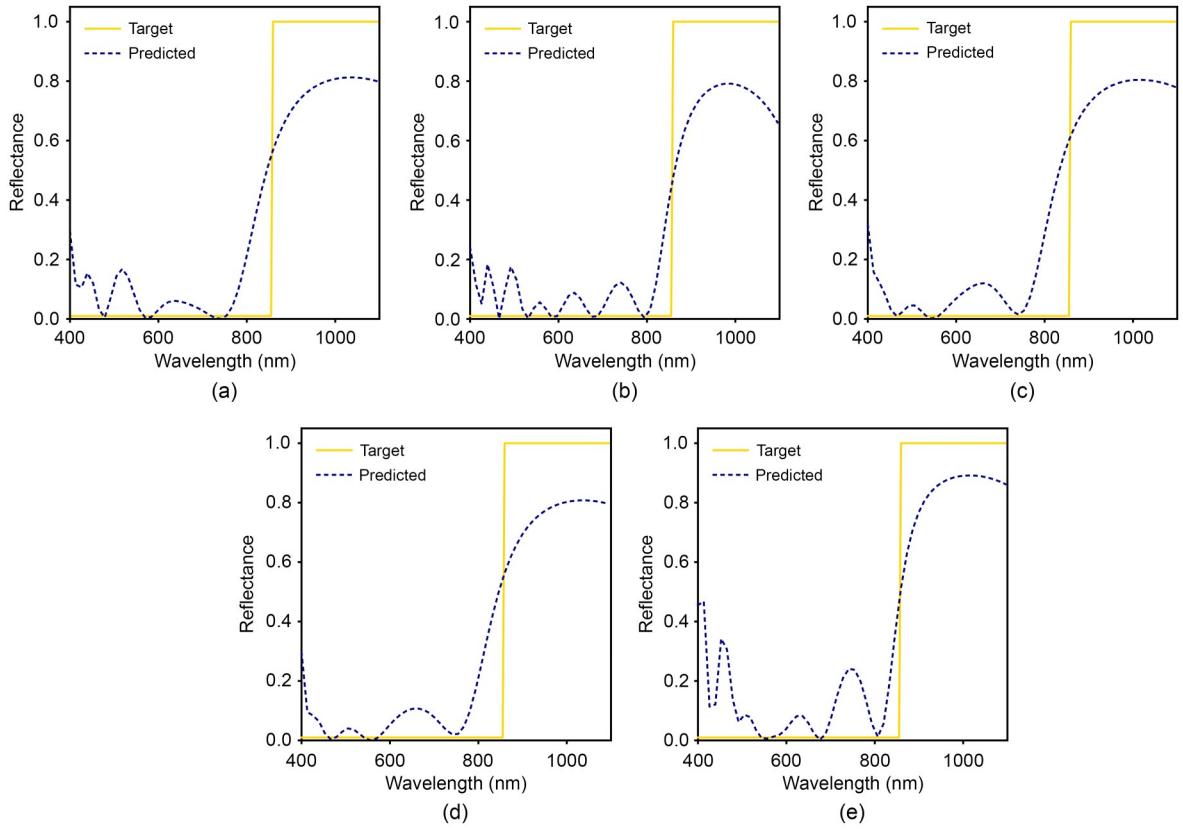


Fig. 6 Performance comparison of reflectance spectra trained with distinct material configurations for the GaAs/Si system at 0° incidence: (a) TiO_2–Al_2O_3–MgF_2; (b) TiO_2–Al_2O_3; (c) TiO_2–MgF_2; (d) TiO_2–SiO_2–MgF_2; (e) TiO_2–SiO_2

(n_H: approximately 2.30) and Al_2O_3 (n_L: approximately 1.70) compared to other pairs such as TiO_2/SiO_2 (n_L: approximately 1.46), which limits the achievable stopband width and reflectance according to thin-film theory.

The J–V curves of the GaAs/Si system under 0° incidence are presented in Fig. 7. The most significant change compared with the reference curves in Fig. 7f is observed in the Si cell. Both the short-circuit current density and the open-circuit voltage of the Si cell are substantially reduced across all filtered configurations in Figs. 7a–7e. This performance drop is fundamentally attributed to the Si cell only receiving the reflected portion of the solar spectrum after the light reaches the filter. In addition, the filter in Fig. 7b resulted in the lowest short-circuit current density of the Si cell; this poor performance strongly correlates with its spectral response, which exhibited roll-off in the long-wavelength region, as shown in Fig. 6b. Since the Si cell relies on the reflected portion of the spectrum, the pronounced drop in filter reflectance directly translates to a critically reduced photon flux density transmitted to the Si absorber, consequently curtailing its output current.

For the GaAs part, a marginal decrease in performance, particularly in short-circuit current, is also evident compared with the independent operation shown in Fig. 7f. This minor degradation stems from the fact that the filter's reflectance in the intended transmission band is not perfectly 0, as presented by the spectral oscillations in Fig. 6. A comparison among the material configurations reveals that TiO_2–SiO_2 achieves the most favorable overall performance at 0° incidence, yielding a total power density of 0.021 W/cm^2. This superior performance can be directly attributed to the filter's spectral characteristics (Fig. 6e). First, the filter exhibits an extremely sharp transition at the band edge. Second, the filter achieves the highest reflectance in the reflection band (long-wavelength region) compared to the other configurations. Furthermore, to evaluate the angular robustness of the designed filters, we extended our analysis to 45° incidence, and the filters' reflectance spectra and the systems' J–V curves with a 45° incidence can be found in Figs. S7 and S8 of the ESM.

The total power density comparison for the GaAs/Si system is summarized in Fig. 8, which presents

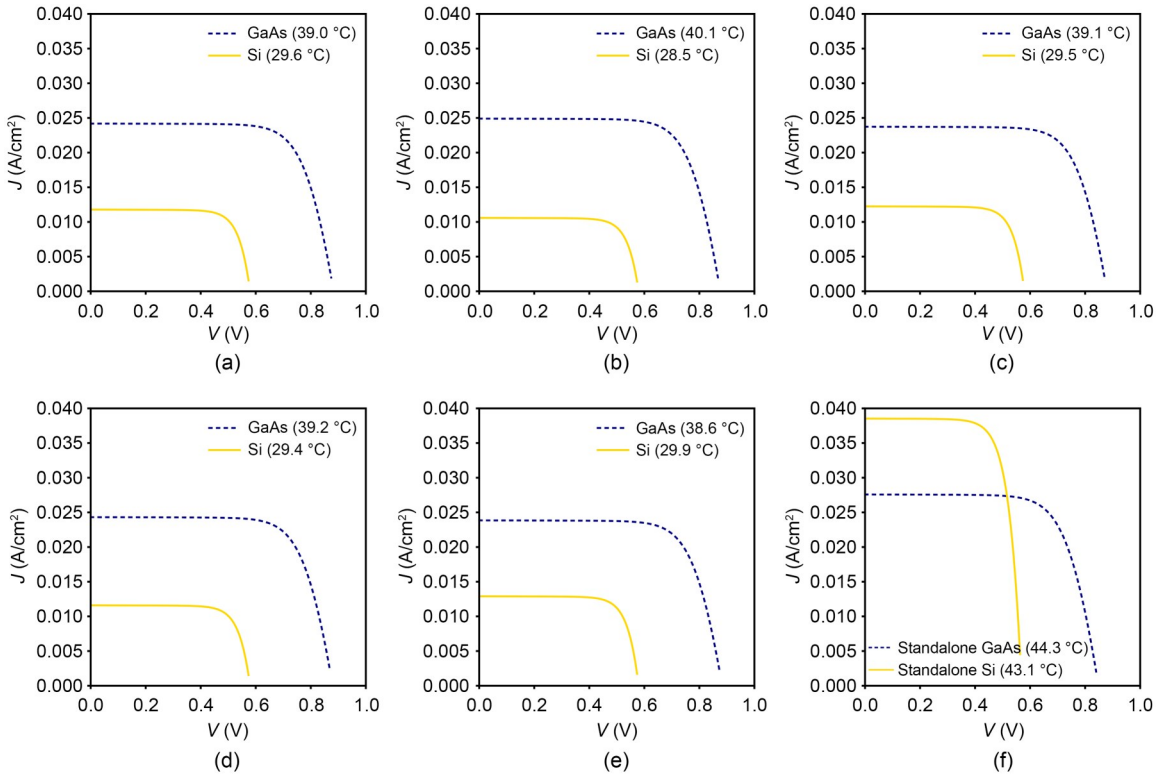


Fig. 7 *J–V* curves of GaAs/Si combined solar cells under AM1.5G conditions using different spectrum splitters: (a) TiO_2–Al_2O_3–MgF_2; (b) TiO_2–Al_2O_3; (c) TiO_2–MgF_2; (d) TiO_2–SiO_2–MgF_2; (e) TiO_2–SiO_2; (f) standalone *J–V* curves of GaAs and Si as a reference. AM1.5G refers to the direct and scattered irradiation spectrum of sunlight when the path length it travels through the atmosphere is approximately 1.5 times that of when it is incident perpendicularly

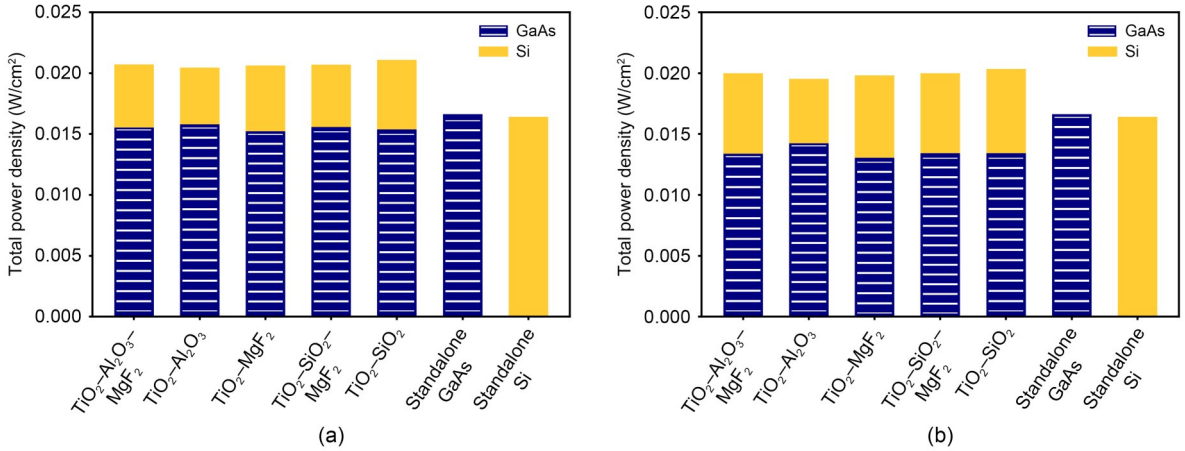


Fig. 8 Total output power density of the GaAs/Si combined system using different spectral-splitting filters with (a) 0° and (b) 45° incidences to the splitter

results for both 0° (Fig. 8a) and 45° (Fig. 8b) incidences. A crucial finding is that the implementation of the spectral-splitting approach leads to a clear performance enhancement at both incidences, as the total power densities for all five hybrid systems surpass the power output of both the standalone GaAs and standalone Si reference cells. This confirms the spectral-splitting efficacy for improved energy harvesting, and importantly, demonstrates the robustness of the system against variations in the incidence. At a 45° incidence, the TiO_2–SiO_2-filtered GaAs/Si system achieves a total efficiency of 20.4%, representing a 22.4% relative

improvement over standalone GaAs (16.63%). The relatively modest decrease in total efficiency from 0° to 45° (approximately 3.5% for TiO_2–SiO_2) indicates that the designed filters possess excellent angular tolerance, which is a critical requirement for practical deployment.

4.3.2 GaInP/Si system performance

For the GaInP/Si system, the fundamental spectral characteristics of the five reoptimized filters remain broadly similar to the previous set designed for GaAs/Si. However, two main spectral features stand out. First, unlike the previous set, all five configurations now exhibit a universal reflectance roll-off in the far long-wavelength region. Second, regarding the key performance metric of spectral separation, the filters in Figs. 9c and 9d (TiO_2–MgF_2 and TiO_2–SiO_2–MgF_2) achieve the most desirable response at 0° incidence, displaying the steepest transition at the cut-off wavelength, which is crucial for maximizing current matching in the GaInP/Si system.

The *J*–*V* curves of the GaInP/Si system at 0° incidence (Fig. 10) mirror the general trends observed in the GaAs/Si system. Specifically, the least impact on the short-circuit current of the GaInP cell is seen in configurations TiO_2–MgF_2 and TiO_2–SiO_2–MgF_2. This is a direct validation of the previous spectral analysis, confirming that the steepest band edge transitions achieved by filters TiO_2–MgF_2 and TiO_2–SiO_2–MgF_2 lead to a minimal photon loss in the passband. The TiO_2–MgF_2 configuration achieves the highest total power density of 0.024 W/cm^2 at 0° incidence, representing a remarkable relative enhancement of 41.9% compared to the standalone GaInP cell (0.017 W/cm^2) and 46.6% compared to the standalone Si cell (0.016 W/cm^2).

At 45° incidence, the GaInP/Si system maintains strong performance, with the TiO_2–SiO_2–MgF_2 configuration achieving the highest total power density of 0.022 W/cm^2 (Fig. S9 of the ESM). This corresponds to a relative efficiency enhancement of 32.3% over standalone GaInP and 36.8% over standalone Si, respectively.

The total power density comparison for both incidence angles is presented in Fig. 11, which unequivocally validates the significant advantage of the GaInP/Si

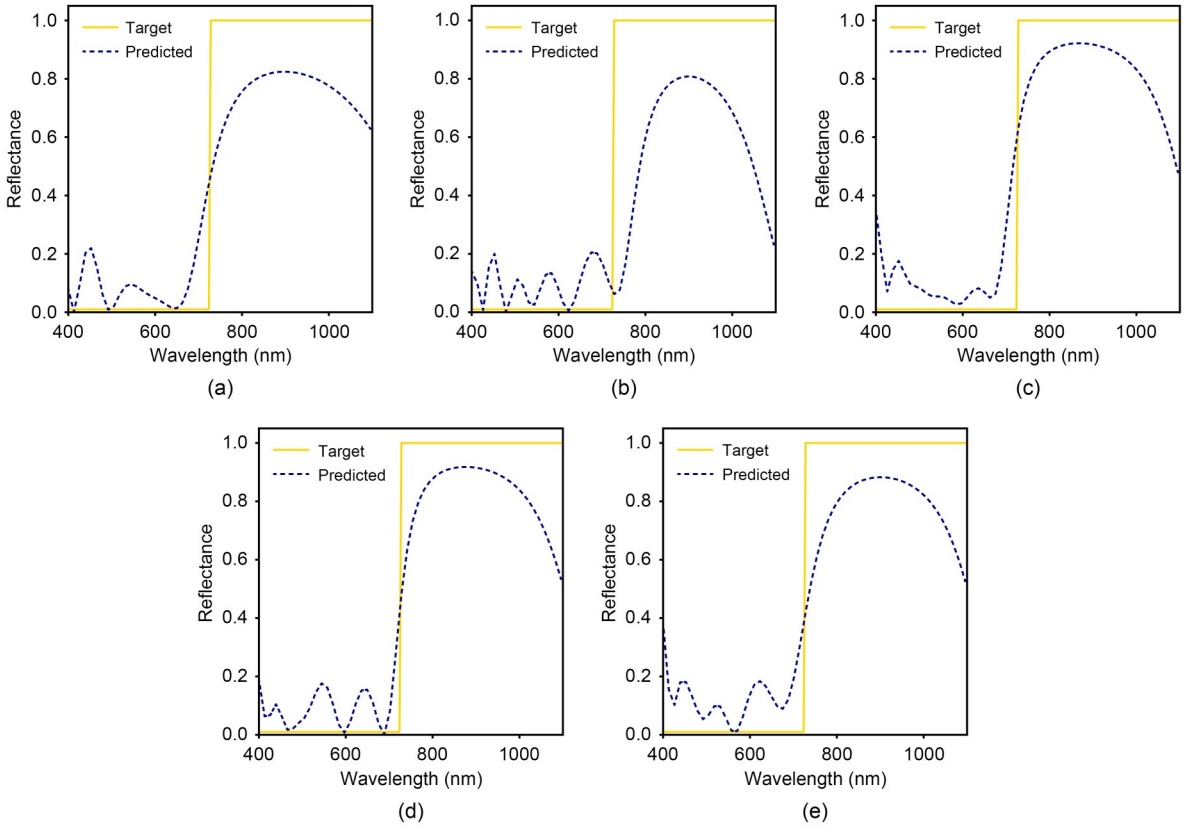


Fig. 9 Performance comparison of reflectance spectra trained with distinct material configurations for the GaInP/Si system at 0° incidence: (a) TiO_2–Al_2O_3–MgF_2; (b) TiO_2–Al_2O_3; (c) TiO_2–MgF_2; (d) TiO_2–SiO_2–MgF_2; (e) TiO_2–SiO_2

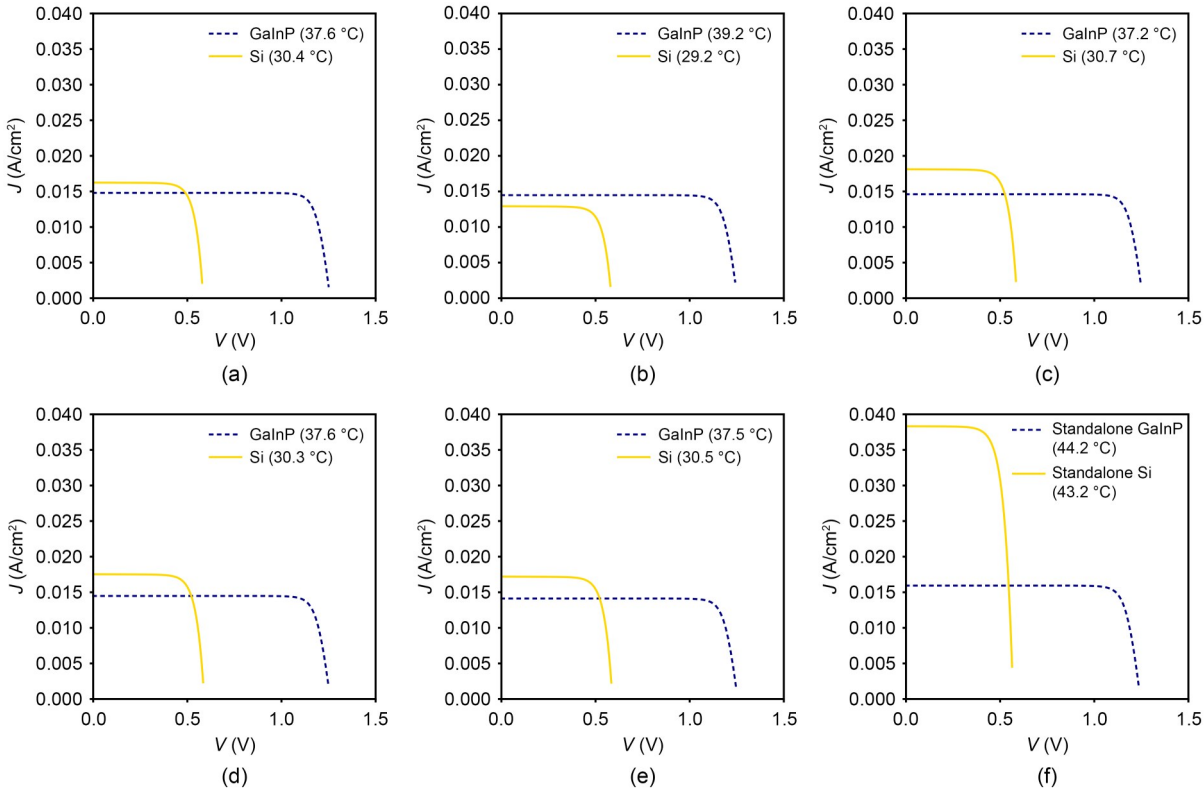


Fig. 10 *J–V* curves of GaInP/Si combined solar cells under AM1.5G conditions using different spectrum splitters: (a) TiO_2–Al_2O_3–MgF_2; (b) TiO_2–Al_2O_3; (c) TiO_2–MgF_2; (d) TiO_2–SiO_2–MgF_2; (e) TiO_2–SiO_2; (f) standalone *J–V* curves of GaInP and Si as a reference

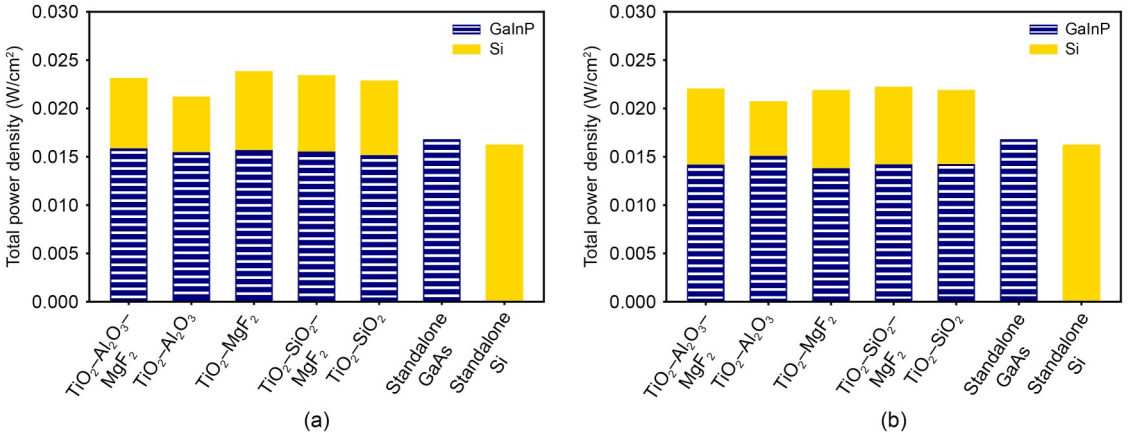


Fig. 11 Total output power density of the GaInP/Si combined system using different spectral-splitting filters with (a) 0° and (b) 45° incidences to the splitter

system. The total power output of all five filtered configurations exceeds that of both the standalone GaInP and Si cells at both 0° and 45° incidences, confirming the efficacy and angular robustness of the methodology. Furthermore, the overall efficiencies with all five filters are relatively 20.0% higher than the efficiency of a standalone GaInP cell.

4.3.3 Thermal performance analysis

An important advantage of the spectral-splitting configuration is the reduction in the operating temperature of the photovoltaic cells, which directly translates to improved conversion efficiency and enhanced long-term reliability. In our thermal analysis, we assume

that each photovoltaic cell reaches thermal equilibrium under illumination, with the cell temperature determined by the balance between absorbed optical power and radiative/convective heat dissipation to the ambient environment at 25 °C.

The temperature reduction achieved by the spectral-splitting configuration is summarized in Fig. 12. For the GaAs/Si system (Fig. 12a), the high-bandgap GaAs cell exhibits a temperature reduction of 4.2–5.7 °C at 0° incidence and 4.4–5.9 °C at 45° incidence across all filter configurations. More dramatically, the low-bandgap Si cell benefits from an exceptional temperature reduction of 13.3–14.6 °C at 0° incidence and 12.8–14.6 °C at 45° incidence. This substantial cooling effect for the Si cell arises because it only receives the reflected long-wavelength portion of the spectrum, significantly reducing its thermal load.

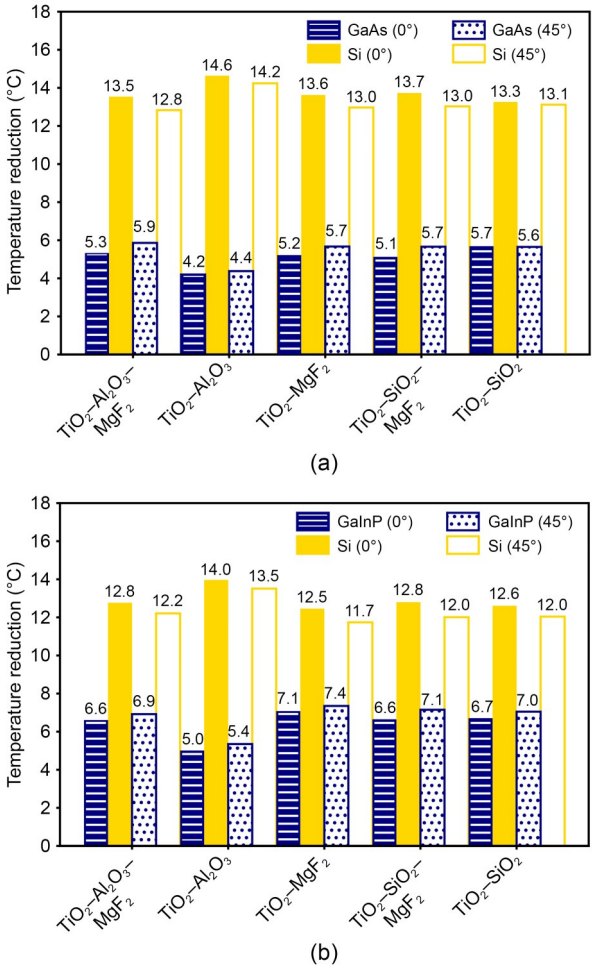


Fig. 12 Temperature reductions of the (a) GaAs/Si and (b) GaInP/Si combined systems using different spectral splitting filters with 0° and 45° incidences to the splitter

For the GaInP/Si system (Fig. 12b), similar trends are observed. The high-bandgap GaInP cell achieves temperature reductions of 5.0–7.1 °C at 0° incidence and 5.4–7.4 °C at 45° incidence. The low-bandgap Si cell again shows the most significant benefit, with temperature reductions ranging from 12.5 to 14.0 °C at 0° incidence and 12.0 to 13.5 °C at 45° incidence. These results highlight a critical advantage of the spectral-splitting architecture: by dividing the solar spectrum between two separate cells, each cell absorbs less thermal energy than a single cell exposed to the full spectrum, resulting in substantially lower operating temperatures and consequently higher conversion efficiencies.

4.3.4 Comparison with conventional 1D-PhCs

Fig. 13 compares the spectral-splitting performance of the PINN-designed TiO_2–MgF_2 photonic crystal against conventional 1D-PhC structures from the literature, encompassing both reflective/transmissive and reflective/absorptive configurations. In the short-wavelength region, the TiO_2–MgF_2 design demonstrates substantially lower reflectance (predominantly below 0.1) compared to previous works 2 and 3, which exhibit reflectance exceeding 0.1, indicating superior optical discrimination. The spectral transition at the cut-off wavelength is considerably sharper than that observed in previous work 1, while in the long-wavelength region, the reflectance remains comparable to existing designs, albeit with a modest decrease beyond 1000 nm.

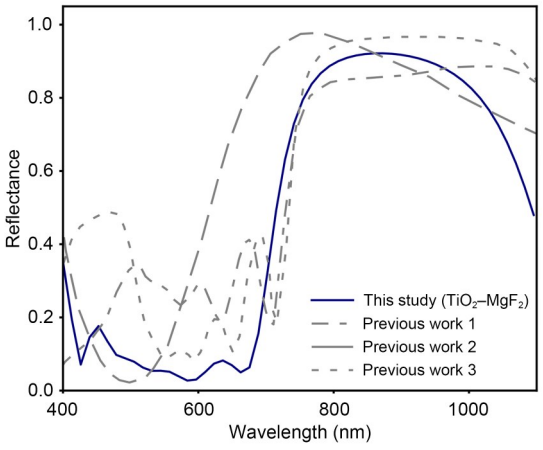


Fig. 13 Comparison of the reflectance between this study (TiO_2–MgF_2), optical coating (previous study 1) from Wei et al. (2025), and 1D-PhCs (previous studies 2 and 3) from Wei et al. (2021)

5 Conclusions

In this study, we introduced a highly efficient and material-aware inverse design framework for 1D-PhCs based on the PINN. By embedding a differentiable TMM as a physical constraint, our method circumvents the need for large labeled data and enables rapid design directly from target spectra. Our key innovation lies in the MOPE approach, where a library of PINN models, each specializing in a different material combination, is pretrained. This paradigm shifts the inverse design process from simple structural optimization to a more powerful and material-aware inverse design. Analysis demonstrated that the PINN model significantly outperforms a traditional data-driven CNN, reducing the validation loss by 54.5% while converging much faster. The practical power of the MOPE framework was showcased by designing a spectral-splitting filter for a tandem photovoltaic system. By deploying five pretrained material-specific models, we rapidly compared design outcomes and identified the optimal material system that maximized the photovoltaic power output, achieving total relative efficiency enhancements of 22.4% and 41.9% compared with standalone GaAs and GaInP cells, respectively. The designed filters demonstrate exceptional incident robustness, maintaining over 20.0% relative efficiency improvement even at 45° incidence with merely 3.5% performance degradation, and effectively reduce the operating temperature of low-bandgap cells by 12.8–14.6 ℃, thereby enhancing the long-term reliability. This result highlights the MOPE framework's capability to solve complex and real-world engineering problems efficiently. While the current demonstration focuses on conventional low-loss dielectrics to establish a fabrication-friendly baseline, we acknowledge that the bandwidth of pure Bragg reflectors is fundamentally constrained by the available refractive index contrast and the absence of resonant phase accumulation. To transcend these limitations, future iterations of the MOPE framework will integrate "expert" models for plasmonic metamaterials, lossy or dispersive nanocomposites, and high-index-contrast metasurfaces.

Acknowledgments

This work is supported by the National Natural Science Foundation of China (No. 52576233) and the Shenzhen Science and Technology Program (Nos. KCXST20221021111609024, KCXFZ20211020165004006, and JCYJ20220818103010021), China.

Author contributions

Haoming LI designed the research and wrote the first draft of the manuscript. Zhiyuan ZHOU, Xinzi LIN, and Wuyong QU processed the corresponding data. Dongxu JI helped to organize the manuscript. Haoming LI and Dongxu JI revised and edited the final version.

Conflict of interest

Haoming LI, Zhiyuan ZHOU, Xinzi LIN, Wuyong QU, and Dongxu JI declared that they have no conflicts of interest.

Declaration on the use of generative AI tools

During the preparation of this work, the authors used Kimi and Deepseek to improve language and readability. After using these tools, the authors reviewed and edited the content as needed and take full responsibility for the content of the publication.

Data availability

The data that support the findings of this study are available from the corresponding author upon reasonable request.

References

Ahmadi M, Pagano R, Matera F, et al., 2025. Analysis of light collection in GaAs/Si HJT four-terminal solar cell system based on spectral splitting and polymeric wedged optics: a role for diffusive lateral supports. *Solar Energy*, 301: 113934. https://doi.org/10.1016/j.solener.2025.113934

Ahmed I, Jeon G, Piccialli F, 2022. From artificial intelligence to explainable artificial intelligence in industry 4.0: a survey on what, how, and where. *IEEE Transactions on Industrial Informatics*, 18(8):5031-5042. https://doi.org/10.1109/TII.2022.3146552

Anzengruber SW, Klann E, Ramlau R, et al., 2012. Numerical methods for the design of gradient-index optical coatings. *Applied Optics*, 51(34):8277-8295. https://doi.org/10.1364/AO.51.008277

Chen YY, Dal Negro L, 2022. Physics-informed neural networks for imaging and parameter retrieval of photonic nanostructures from near-field data. *APL Photonics*, 7(1): 010802. https://doi.org/10.1063/5.0072969

Chen YY, Lu L, Karniadakis GE, et al., 2020. Physics-informed neural networks for inverse problems in nano-optics and metamaterials. *Optics Express,* 28(8):11618-11633. https://doi.org/10.1364/OE.384875

Dorodnyy A, Shklover V, Braginsky L, et al., 2015. High-efficiency spectrum splitting for solar photovoltaics. *Solar Energy Materials and Solar Cells*, 136:120-126. https://doi.org/10.1016/j.solmat.2015.01.005

Hecht E, 2021. Optics. 5th Edition. Addison-Wesley, Reading, USA.

Hong Y, Nicholls DP, 2022. Data-driven design of thin-film optical systems using deep active learning. *Optics Express*,

30(13):22901-22910.
https://doi.org/10.1364/OE.459295

Jiang YJ, Keevers MJ, Pearce P, et al., 2019. Design of an intermediate Bragg reflector within triple-junction solar cells for spectrum splitting applications. *Solar Energy Materials and Solar Cells*, 193:259-269.
https://doi.org/10.1016/j.solmat.2019.01.011

Jiménez-Luna J, Grisoni F, Schneider G, 2020. Drug discovery with explainable artificial intelligence. *Nature Machine Intelligence*, 2(10):573-584.
https://doi.org/10.1038/s42256-020-00236-4

Khatib O, Ren SM, Malof J, et al., 2022. Learning the physics of all-dielectric metamaterials with deep Lorentz neural networks. *Advanced Optical Materials*, 10(13):2200097.
https://doi.org/10.1002/adom.202200097

Kim M, Seo J, Yoon S, et al., 2021. Optimization and performance analysis of a multilayer structure for daytime radiative cooling. *Journal of Quantitative Spectroscopy and Radiative Transfer*, 260:107475.
https://doi.org/10.1016/j.jqsrt.2020.107475

Lee I, Kim C, Ju K, et al., 2023. Implementation of particle swarm optimization for complete inverse design of multilayered optical filters. *Applied Optics*, 62(34):8994-9001.
https://doi.org/10.1364/AO.500775

Li HM, Wan SB, Wang L, et al., 2025. Divide and conquer: spectral-splitting and utilization of thermal radiation from waste heat in the steel industry. *Applied Energy*, 378:124836.
https://doi.org/10.1016/j.apenergy.2024.124836

Li JL, Jiang Y, Liu J, et al., 2024. A photosynthetically active radiative cooling film. *Nature Sustainability*, 7(6):786-795.
https://doi.org/10.1038/s41893-024-01350-6

Lininger A, Hinczewski M, Strangi G, 2021. General inverse design of layered thin-film materials with convolutional neural networks. *ACS Photonics*, 8(12):3641-3650.
https://doi.org/10.1021/acsphotonics.1c01498

Liu DJ, Tan YX, Khoram E, et al., 2018. Training deep neural networks for the inverse design of nanophotonic structures. *ACS Photonics*, 5(4):1365-1369.
https://doi.org/10.1021/acsphotonics.7b01377

Liu GW, Chen SJ, Lin CY, 2024. Optimization of dielectric-metal multilayer structure for color-preserving radiative cooling window. *ACS Omega*, 9(28):30425-30435.
https://doi.org/10.1021/acsomega.4c01792

Luce A, Mahdavi A, Marquardt F, et al., 2022. TMM-Fast, a transfer matrix computation package for multilayer thin-film optimization: tutorial. *Journal of the Optical Society of America A*, 39(6):1007-1013.
https://doi.org/10.1364/JOSAA.450928

Luce A, Mahdavi A, Wankerl H, et al., 2023. Investigation of inverse design of multilayer thin-films with conditional invertible neural networks. *Machine Learning: Science and Technology*, 4(1):015014.
https://doi.org/10.1088/2632-2153/acb48d

Ma TG, Wang HZ, Guo LJ, 2024. OptoGPT: a foundation model for inverse design in optical multilayer thin film structures. *Opto-Electronic Advances*, 7(7):240062.
https://doi.org/10.29026/oea.2024.240062

Ma XL, Li X, Wang Y, 2025. One-dimensional Si/SiO_2 photonic crystal filters for $Ga_xIn_{1-x}As_ySb_{1-y}$ thermophotovoltaic devices. *Journal of the Optical Society of America B*, 42(12):2740-2746.
https://doi.org/10.1364/JOSAB.575204

Medvedev V, Erdmann A, Rosskopf A, 2025. Physics-informed deep learning for 3D modeling of light diffraction from optical metasurfaces. *Optics Express*, 33(1):1371-1384.
https://doi.org/10.1364/OE.544116

Molesky S, Lin Z, Piggott AY, et al., 2018. Inverse design in nanophotonics. *Nature Photonics*, 12(11):659-670.
https://doi.org/10.1038/s41566-018-0246-9

Pavlichenko I, Broda E, Fukuda Y, et al., 2015. Bringing one-dimensional photonic crystals to a new light: an electro-photonic platform for chemical mass transport visualisation and cell monitoring. *Materials Horizons*, 2(3):299-308.
https://doi.org/10.1039/C4MH00195H

Pedreschi D, Giannotti F, Guidotti R, et al., 2019. Meaningful explanations of black box AI decision systems. Proceedings of the 33rd AAAI Conference on Artificial Intelligence, p.9780-9784.
https://doi.org/10.1609/aaai.v33i01.33019780

Qu WY, Li HM, Li GY, et al., 2025. Genetic algorithm-driven design of a spectral-splitting filter for a high-efficiency hybrid photovoltaic-thermoelectric system. *Case Studies in Thermal Engineering*, 75:107255.
https://doi.org/10.1016/j.csite.2025.107255

Rahman RU, Yousuf H, Khokhar MQ, et al., 2025. Optimized current and voltage matching in high-efficiency bifacial III−V/silicon multijunction solar cells with enhanced spectral albedo. *Sustainable Energy Technologies and Assessments*, 77:104332.
https://doi.org/10.1016/j.seta.2025.104332

Riganti R, Zhu YL, Cai W, et al., 2025. Multiscale physics-informed neural networks for the inverse design of hyperuniform optical materials. *Advanced Optical Materials*, 13(16):2403304.
https://doi.org/10.1002/adom.202403304

Ruan ZH, Yuan Y, Zhang XX, et al., 2016. Determination of optical properties and thickness of optical thin film using stochastic particle swarm optimization. *Solar Energy*, 127:147-158.
https://doi.org/10.1016/j.solener.2016.01.027

Rühle S, 2016. Tabulated values of the Shockley–Queisser limit for single junction solar cells. *Solar Energy*, 130:139-147.
https://doi.org/10.1016/j.solener.2016.02.015

Schubert MF, Mont FW, Chhajed S, et al., 2008. Design of multilayer antireflection coatings made from co-sputtered and low-refractive-index materials by genetic algorithm. *Optics Express*, 16(8):5290-5298.
https://doi.org/10.1364/oe.16.005290

Tikhonravov AV, Trubetskov MK, Debell GW, 1996. Application of the needle optimization technique to the design of optical coatings. *Applied Optics*, 35(28):5493-5508.
https://doi.org/10.1364/AO.35.005493

Tikhonravov AV, Trubetskov MK, Debell GW, 2007. Optical coating design approaches based on the needle optimization

technique. *Applied Optics*, 46(5):704-710. https://doi.org/10.1364/AO.46.000704

Wan BF, Zhou ZW, Xu Y, et al., 2021. A theoretical proposal for a refractive index and angle sensor based on one-dimensional photonic crystals. *IEEE Sensors Journal*, 21(1):331-338. https://doi.org/10.1109/JSEN.2020.3013289

Wang HZ, Zheng ZY, Ji CG, et al., 2021. Automated multi-layer optical design via deep reinforcement learning. *Machine Learning: Science and Technology*, 2(2):025013. https://doi.org/10.1088/2632-2153/abc327

Wang JJ, Li YL, Gao RX, et al., 2022. Hybrid physics-based and data-driven models for smart manufacturing: modelling, simulation, and explainability. *Journal of Manufacturing Systems*, 63:381-391. https://doi.org/10.1016/j.jmsy.2022.04.004

Wang QZ, Zhang YS, Burguete-Lopez A, et al., 2024. The transformational dive of nanophotonics inverse design from deep learning to artificial general intelligence. *APL Photonics*, 9(10):100902. https://doi.org/10.1063/5.0226592

Wei D, Cao F, Wu ZX, et al., 2021. Enhanced spectral splitting in a novel solar spectrum optical splitter based on one dimensional photonic crystal heterostructure. *Journal of Materiomics*, 7(3):648-655. https://doi.org/10.1016/j.jmat.2020.10.014

Wei R, Xu TS, Guo CL, 2025. High-efficiency solar hybrid photovoltaic/thermal system enabled by ultrathin asymmetric Fabry–Perot cavity. *ACS Photonics*, 12(2):628-635. https://doi.org/10.1021/acsphotonics.4c01315

You GF, Qian C, Tan SR, et al., 2024. Driving deep-learning-based metasurface design with Kramers-Kronig relations. *Physical Review Applied*, 22(4):L041002. https://doi.org/10.1103/PhysRevApplied.22.L041002

Yu T, Liu RM, Yang ZX, et al., 2025. Color design for daytime radiative cooling: fundamentals and approaches. *Applied Energy*, 377:124436. https://doi.org/10.1016/j.apenergy.2024.124436

Yu ZJ, Fisher KC, Wheelwright BM, et al., 2015. PVMirror: a new concept for tandem solar cells and hybrid solar converters. *IEEE Journal of Photovoltaics*, 5(6):1791-1799. https://doi.org/10.1109/JPHOTOV.2015.2458571

Zhan T, Liu QS, Sun YJ, et al., 2022. A general machine learning-based approach for inverse design of one-dimensional photonic crystals toward targeted visible light reflection spectrum. *Optics Communications*, 510:127920. https://doi.org/10.1016/j.optcom.2022.127920

Zhelyeznyakov M, Fröch J, Wirth-Singh A, et al., 2023. Large area optimization of meta-lens via data-free machine learning. *Communications Engineering*, 2(1):60. https://doi.org/10.1038/s44172-023-00107-x

Zhu L, Lv C, Hua W, et al., 2025. PTLOR-Net: physical transfer learning based optical response prediction network of metasurfaces. *ACS Photonics*, 12(5):2624-2636. https://doi.org/10.1021/acsphotonics.5c00104

Electronic supplementary materials

Sections S1–S12, Tables S1 and S2, Figs. S1–S9